Detection of Weak Doppler Microembolic Signature using Two-Dimensional-Adaptive Time-Frequency Threshold from Spectrogram

Sébastien Ménigot, Maroun Geryes, Jean Marc Girault

Detection of Weak Doppler Microembolic Signature using Two-Dimensional-Adaptive Time-Frequency Threshold from Spectrogram

Sébastien Ménigot[a,b,*], Maroun Geryes[c], Jean-Marc Girault[a,b]

[a] *LAUM, UMR-CNRS 6613, Université du Maine, Le Mans, France*
[b] *ESEO Group, Angers, France*
[c] *Department of Physics and Electronics, Faculty of Sciences I, Lebanese University, Beirut, Lebanon*

Abstract

Prevention of cerebrovascular accidents (CVA) can be achieved by detecting their related precursor signs. A new generation of transcranial Doppler (TCD) systems is presented for detecting the smallest possible microemboli. However, many artefacts appear with these mono-gated Holter TCDs. Thus, the aim of the method becomes achieving microembolic detection while rejecting artefacts. For the clinicians' procedure, the detection proposed is based on an adaptive thresholding applied on the spectrogram of the Doppler signal. The method required achieving three steps. First, the beginning of each cardiac cycle is assessed from the spectrogram of the Doppler signal. Second, by assuming that the Doppler signal is pseudo-cyclostationary, the spectrogram are segmented and time-normalised into sub-spectrograms for each cardiac cycles. Two two-dimensional-adaptive (2D-adaptive) thresholds of detection for microemboli and artefacts were statistically adjusted in both time and frequency. Third, the microembolus detection consists in both detecting the over-intensities in the sub-spectrograms and checking if the detected signatures are not artefacts. The ROC curve results show that the performances are 3.6 times higher compared to those of the standard detection. The detection rate can be increased by 22% compared to standard detection. Besides, the false alarm rate can be reduced by 28%. Using an 2D-adaptive threshold adjusted in both time and frequency, microemboli of weaker intensity can be detected. The analysis of a long acquisition could be possible, and better support of high-risk asymptomatic patient could be considered.

Keywords: Microembolus detection, transcranial Doppler ultrasound, microembolus, spectrogram, artefact rejection.

DOI: https://doi.org/10.1016/j.bspc.2019.101811
Conflict of interest: none.

Highlights

- Detection of weak Doppler microembolic signals
- Detector based on two-dimensional-adaptive threshold computed from time-normalised sub-spectrograms of each cardiac cycle.
- Including an artefact rejection to take into account features of mono-gated Holter transcranial Doppler system.
- Concept proof validated on clinical data.

*ESEO Group, 10 boulevard Jeanneteau, CS 90717, 40107 Angers CEDEX 2, France
Email addresses: sebastien.menigot@eseo.fr (Sébastien Ménigot), maroungeryes@gmail.com (Maroun Geryes), jean-marc.girault@eseo.fr (Jean-Marc Girault)

1. Introduction

Despite improvements in prevention, in risk factor management, in treatment and care, cerebrovascular accidents (CVA) remain the second cause of mortality in Europe, responsible for about 154 deaths per 100,000 inhabitants each year [1]. The cost of direct healthcare and the indirect loss is estimated at around 45 billion euros in the European Union [2]. One of the main reasons of ischemic strokes is microemboli circulating in the cerebral vascular system and originating from carotid and aortic plaques or cardiac sources [3]. Therefore, microembolus detection has become a public health issue. In risk factor management and diagnosis, the transcranial Doppler system (TCD) is the unique non-invasive and non-irradiant device for detecting the spontaneous circulating cerebral microemboli [4, 5]. From TCD systems, these microembolic events appear as high-intensity transient signals (HITS) superimposed on the backscattered TCD signal. Therefore, it can help clinicians in monitoring high-risk asymptomatic patients [6], [7]. Furthermore, since small microemboli are precursors of large embolus with more dangerous effects [8], early detection of the smallest microemboli is a crucial step.

Commercial TCDs for microembolus detection are mostly based on Doppler energy. A constant threshold is empirically set by a clinician over the entire examination. Although such standard detectors perform well for relatively intense embolic signals, their performance in the detection of low-intensity microembolic signals is unsatisfactory. First, the clinician can detect microemboli audibly, while the standard methods remain silent. Second, all TCDs display the spectrogram to help clinicians in manual detection. The clinician can thus detect some inaudible microembolus signatures through using the spectrogram. New detectors should take into account this time-frequency information. Moreover, to detect higher numbers of small microemboli, the examination duration has to be increased, due to the low number of events occurring per hour. Unfortunately, commercially used TCD systems have found several restrictions including lengthy procedures for probe positioning, unreliable microembolus detection, and short examination durations. To overcome these drawbacks, new TCDs, such as Holter, have offered the possibility of servo-controlled positioning of the ultrasound probe and prolonged patient monitoring (exceeding several hours) [9], with the microembolus detection performed offline. Note that Holter TCD can only record data on a mono-gate. However, the servo-controlled probe positioning results in a great increase in the number of signal artefacts. These artefacts can be misinterpreted as true microembolic signals and thus can greatly mislead the embolus detection system. Therefore, the development of new microemboli detectors should also take into consideration the artefact features of Holter signals. Artefact rejection becomes a necessary step engaged in the whole detection process. To sum up, a good detector should take into account the time-frequency information in the cardiac cycle and should include an artefact rejection technique.

Several methods have combined microembolus detection and artefact rejection. Among the artefact rejection methods, some of them are based on features derived from detected patterns: time interval and frequency of the detection [10], intensity [11] or parameters of fractional Fourier transform [12]. Other methods are based on multigate systems [3, 13]. Instead of mixing artefact rejection and microembolus detection, some methods have been focused only on microembolus detection without covering artefact rejection. The basic concern related to all detectors is the separation of the information related to microemboli from the cardiac flow information. Most of the microembolus detection can be separated into two main families. The first one consists of filtering cardiac flow information through a frequency decomposition. In [11, 14], wavelet decomposition can solve the compromise between temporal and frequency resolutions in the detection. The second one consists of making a time-varying threshold based on cardiac flow information. In [15], the detection was improved by the combination of an adaptive threshold and a neuro-fuzzy detector. In [16], the adaptive threshold is assessed from energy fluctuation. Note that other solutions were proposed either based on the transmitter coding of the Doppler system [17], or on model breaking detection of Doppler signals [18] or high order statistics [19]. However, since an artefact rejection technique was not included in these last methods, these automatic detection methods are not implemented in commercial devices. Nevertheless, some detectors have improved the detection rate by partially using the criteria of a good detector previously explained (*i.e.* using time-frequency information). Thanks to the pseudo-cyclostationarity properties of the blood Doppler signal [20], data of each cardiac cycle have been segmented [21] or the threshold can be adaptive with the cardiac cycle [22]. Finally, an image processing approach has been performed through the time-frequency repre-

sentation of the Doppler signal [23]. However, this technique requires guaranteeing the Gaussian property of the Doppler speckle in the Doppler signal. Moreover, the artefact rejection requires a machine learning for the classification, which can be difficult according to the data quality and the learning data amount.

In this paper, we proposed an original offline detection based on the time-frequency representation of the Doppler signal and designed for features of mono-gated TCD Holter system. The aim was to detect microemboli combined with an artefact rejection. We merged the advantage of both the image processing approach [23] and the segmented approach [21]. The novelty of this work lies in the following items:

- the sensitivity of the detection varies with the frequency and the position in the cardiac cycle [24]. The method uses spectrogram segments (or sub-spectrograms) of the same duration (time-normalisation with a resampling step) and starting with the position in the cardiac cycle (systolic peak for instance). From these time-normalised sub-spectrograms, a two-dimensional threshold can be adjusted in time and frequency;
- the microembolus detection and the artefact rejection are self-adjusted for each patient and every five minutes;
- in contrast with most previous methods, no assumption on noise property is required and artefact rejection (even simple) is included.

This study focuses on the feasibility of such detection. The detection method is applied to a signal database acquired by a mono-gated Holter TCD in patients with carotid stenosis. The first step is to set the method in the first part of the database. The second step was to check the detection performance blindly in the second part of the database. Finally, the detection results are compared to the standard method.

2. Materials and Methods

As explained above, the detection method is based on a two-dimensional-adaptive (2D-adaptive) thresholding constructed from sub-spectrograms for which the duration of the cardiac cycle are normalised, following the flow chart shown in Fig. 1; a more detailed flow chart describing this process is reported in the appendix. As a first step, after computing the whole spectrogram from the Doppler signal, the time boundaries of each cardiac cycle are assessed. By assuming that the Doppler signal is pseudo-cyclostationary, due to the pseudo-regularity of the cardiac rhythm, sub-spectrograms (*i.e.* segments of spectrogram) are segmented and extracted following the duration of the cardiac cycles. Then, they are normalised in time to ensure that all sub-spectrograms have the same number of samples. In the second step, from all these time-normalised sub-spectrograms, two 2D-adaptive thresholds of microembolus detection and artefact rejection were adjusted in time and frequency from statistics derived from sub-spectrograms. Finally, in the third step, the microembolus detection consists in detecting the over-intensities of the time-normalised sub-spectrograms and in checking if the detections are not artefacts.

2.1. Clean Spectrogram

Following step 1 in the flow chart in Fig. 1, the input of the detector is based on the spectrogram $S(\mathbf{y}, n, f)$ of the Doppler signal $\mathbf{y}(n)$:

$$S(\mathbf{y}, n, f) = \left| \sum_{k=0}^{N-1} \mathbf{y}(k) g^*(n-k) \mathrm{e}^{-j2\pi f \frac{k}{N}} \right|^2 . \quad (1)$$

where n is the discrete time, f the frequency, * the symbol of the complex conjugate, $g(n)$ the Hamming apodisation window of N-width. Note that the Doppler signal $\mathbf{y}$ must be stationary in the apodisation window. This hypothesis is considered true for a duration of around 10 ms [25]. Therefore N has to be set according to the sampling frequency. As illustration, Fig. 2a shows an example of a spectrogram computed from a 3.5-second Doppler signal.

Furthermore, in order to determine the blood flow direction, the Doppler signal $\mathbf{y}(n)$ is a complex IQ signal where the signal of the positive frequencies $f_\oplus$ (forward flow approaching the transducer) can be different from the signal of the negative frequencies $f_\ominus$ (backward flow moving away from the transducer). Nevertheless, for strong over-intensities (over-driving electronics) and/or because of interference problems between the I and Q channels (*e.g.* crosstalk), I-channel can physically disrupt Q-channel (and reciprocally Q-channel on I-channel) on the electronic board. This disturbance is observed at the same time by similar, even the same, signatures on the spectrogram for the positive and negative frequencies (*i.e.* spectrum of the positive frequencies $\approx$ spectrum of the negative

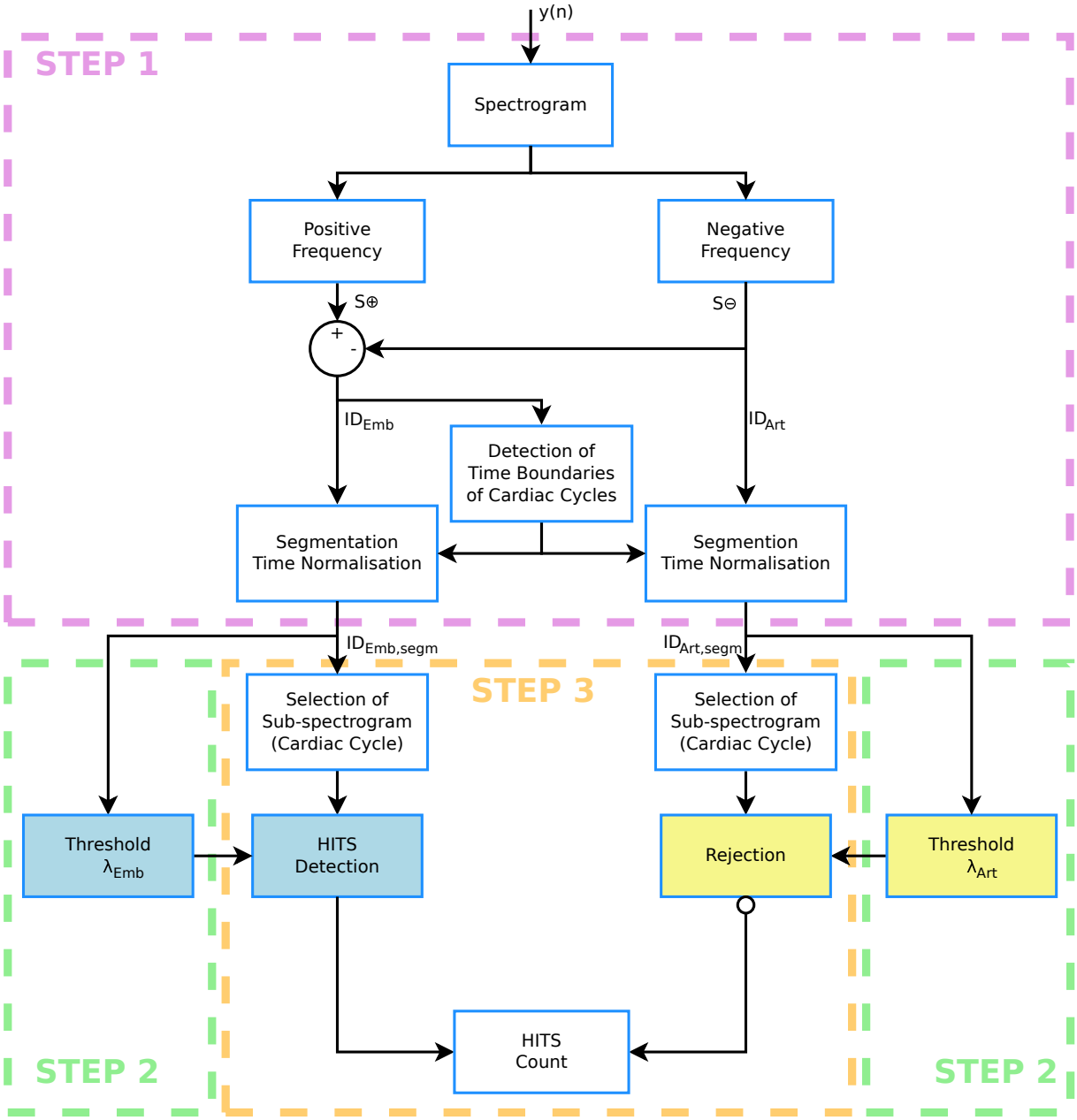

Figure 1: Block diagram representing microembolus detection from the spectrogram. The process is divided into 3 steps: (1) computing of the clean time-normalised sub-spectrograms $ID_{Emb,segm}(n,f)$ and the time-normalised sub-spectrograms $ID_{Art,segm}(n,f)$, (2) computing the adaptive thresholds $\lambda_{Emb}(n,f)$ and $\lambda_{Art}(n,f)$ and (3) thresholding with equation 2.

frequencies). This could lead to creating artefacts which mainly appear as bidirectional[1] [14, 26, 27].

[1]Since an energy on positive (or respectively negative) Doppler frequencies is associated when the blood flow approaches (or respectively moving away) the probe, a signature in both the positive and negative frequencies would mean that an object is travelling in both opposite directions at the same time. This event has no physical meaning, that is why it is called bidirectional artefact.

Taking into consideration the mono-gate property of the Holter TCD, an efficient solution to reduce bidirectional artefacts simply consists in computing a simple difference between the spectra from positive and negative frequencies (example in Fig. 2c). Removing artefacts is equivalent to clean the spectrograms. However, this simple subtraction of the spectra is valid only if no energy of blood flow exists in the negative frequencies (example of spectrogram

for negative frequencies in Fig. 2b). Therefore, in this method, we assume that the clinician sets the probe to obtain the blood flow in the positive frequencies only (example of spectrogram for positive frequencies in Fig. 2a). This implies that there is no energy coming from the backward flow, *i.e.* measured in the negative frequencies (example of spectrogram for negative frequencies in Fig. 2b). Thus, the signatures in the negative frequencies are only related to artefacts, while the signatures in the positive frequencies are related to both blood flow and artefacts. Therefore, a clean spectrogram $ID_{Emb}(n,f)$ for the microembolus detection and a spectrogram $ID_{Art}(n,f)$ for the artefact rejection, on which the thresholds will be applied, can be obtained:

$$\left\{ \begin{array}{l} ID_{Emb}(n,f) = |S_{\oplus}(\mathbf{y},n,f)| - |S_{\ominus}(\mathbf{y},n,f)|\,; \\ ID_{Art}(n,f) \;\; = |S_{\ominus}(\mathbf{y},n,f)|\,, \end{array} \right. \tag{2}$$

with

$$S_{\oplus}(\mathbf{y},n,f) = \left\{ \begin{array}{l} S(\mathbf{y},n,f)\ ,\ \forall f \geqslant 0; \\ 0\ ,\ \forall f < 0 \end{array} \right. , \tag{3}$$

$$S_{\ominus}(\mathbf{y},n,f) = \left\{ \begin{array}{l} 0\ ,\ \forall f \geqslant 0; \\ S(\mathbf{y},n,f)\ ,\ \forall f < 0. \end{array} \right. . \tag{4}$$

Note that if artefacts are mono-directional in the backward flow, the method could be sightly simplified by deactivating the subtraction such $ID_{Emb}(n,f) = |S_{\oplus}(\mathbf{y},n,f)|$.

2.2. Segmentation and Time Normalisation for Each Cardiac Cycle

As shown in step 2 in the flow chart shown in Fig. 1, by assuming that the Doppler signal $\mathbf{y}$ is pseudo-cyclostationary [20] with the cardiac cycles, then the spectrogram $S_{\oplus}(\mathbf{y},n,f)$ is also considered pseudo-cyclostationary with the cardiac cycles. Using the same reasoning, as the clean spectrogram ID_{Emb} is made from pseudo-cyclostationary $S_{\oplus}(\mathbf{y},n,f)$, the clean spectrogram ID_{Emb} is also considered statistically pseudo-periodic with the cardiac cycles (step 1 in Fig. 1). Therefore, in order to compute the 2D-adaptive thresholds, the clean spectrogram can be (i) segmented by splitting into several sub-spectrograms, *i.e.* one spectrogram segment for each cardiac cycle. Then, (ii) the sub-spectrograms are normalised in time to ensure that all sub-spectrograms have the same number of samples.

The first step of the sub-spectrogram calculation procedure consists in segmenting each cardiac cycle, *i.e.* by finding the beginning and the end of each cardiac cycle from the time-frequency information $ID_{Emb}(n,f)$ (white crosses in Figs. 2c and 3a). This process is illustrated in Fig. 4. This part consists in roughly assessing the maximal Doppler frequency, on which the time boundaries of each cardiac cycle will be assessed. For each spectrum of the spectrogram, the maximal Doppler frequency is assessed by finding the highest frequency among the frequencies for which the amplitude of the spectrogram (as shown in Fig. 4a) is higher than a one-dimensional threshold $\overline{ID_{Emb}}$. This one-dimensional threshold $\overline{ID_{Emb}}$ is computed (Fig. 4c) as an average of the mean spectrum (Fig. 4b). Note that this threshold is the same for all time position n and all frequency f, but it does not allow us to detect microembolus, since it is especially designed to detect the maximal frequency. Therefore, a binary spectrogram (Fig. 4d) can be obtained by thresholding the spectrogram with $\overline{ID_{Emb}}$. For each time n, the maximal positive Doppler frequency $f^{+}_{max}(n)$ (white dotted lines in Figs. 4d) is assessed as the maximal frequency where the binary spectrogram is not equal to zero. To reduce high frequencies in f^{+}_{max}, a short-term average filter is applied on f^{+}_{max} with a window of $N_{smooth} = 8$ samples (from our experience). Note this simple process is similar to a percentile method [28, 29] by using the backscattered power as threshold. This was sufficient for our database, since the main goal of that step is only to extract the periodicity of f^{+}_{max}. Then, the time boundaries t_{HR} of each cardiac cycle are extracted by finding the local maxima (as for example the white crosses on spectrograms shown in Figs. 2c, 3a 4d), using a peak detection algorithm[2] applied on $f^{+}_{max}(n)$ [30]. Note that the algorithm excludes local peak if the duration between two successive boundaries t_{HR} is not physiologically realistic, *i.e.* for a heart rate lower than 180 bpm [31]. However, if a time boundary t_{HR} of a cardiac cycle matches with an artefact, *i.e.* if the median $\text{med}(ID_{Art})$ of the spectrum $ID_{Art}(t_{HR},f)$ is higher than the constant threshold $\lambda_{HR,Art}$, the cardiac cycle will be excluded from the microembolus detection. Note that, from our experience, this constant threshold $\lambda_{HR,Art}$ has been assessed as:

$$\lambda_{HR,Art} = \mathcal{P}\left(ID_{Art}(n,f), \text{erf}\left(\frac{1}{\sqrt{2}}\right)\right),\ \forall n, \forall f, \tag{5}$$

[2]The algorithm is based on looking for the highest point for which there are points lower on both sides (left and right) of this highest point.

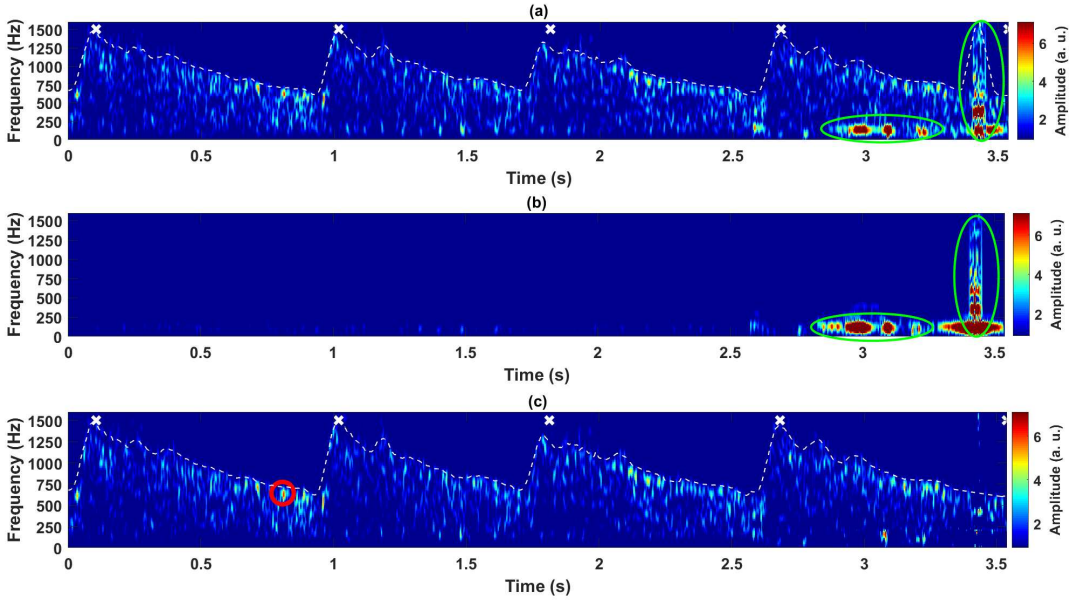

Figure 2: Example of a spectrogram computed from a Doppler signal $\mathbf{y}$. (a) Spectrogram $|S_{\oplus}|$ for the positive frequencies. (b) Spectrogram $|S_{\ominus}|$ for the negative frequencies. Note that this spectrogram ID_{Art} is also the artefact rejection procedure. (c) Clean spectrogram ID_{Emb} for microembolus detection. As an illustration, from methods described in section 2.2, the maximal Doppler frequency $f^{+}_{max}(n)$ is depicted by a white line, the time boundaries of cardiac cycles by white crosses. Note also that the color map is the same for all graphs.

where $\mathcal{P}$ denotes the function percentile and $\mathrm{erf}(x) = \frac{2}{\sqrt{\pi}} \int_0^x e^{-t^2}\, \mathrm{d}t$ the error function. Note that the definition of threshold based on the percentile notion is more general than a simple "N times the standard deviation", since it is always true regardless of the distribution (not only for the normal distribution). If the distribution of $ID_{Art}(n, f)$ is Gaussian, the threshold would be equal to x times the standard deviation. This property comes from the "3 sigma law" [32], where $\mathrm{erf}(x/\sqrt{2})$ is related to x-standard deviation. Finally, the valid cardiac cycles that are kept are those having time boundaries without artefacts and those being physiologically realistic.

In the second step of the sub-spectrogram extraction procedure, shown in Fig. 3, knowing the time boundaries of cardiac cycles, a sub-spectrogram can be extracted for each valid cardiac cycle (as for example in Figs. 3b, d, f), *i.e.* a spectrogram limited by the systolic peak of the current cardiac cycle and the systolic peak of the next cardiac cycle. If the cardiac rhythm is constant, each cardiac cycle would have the same number of samples (because of the same duration) and the spectrogram would be already normalised in time. However, as cardiac cycles have variable durations but with the same size in frequency, the sub-spectrograms have to be normalised in time by resampling in time exclusively (as respectively shown in Figs. 3c, e, g). Note that this resampling is only applied in the time, since every spectrum constituting the spectrogram has the same size in frequency. For each frequency f of a sub-spectrogram (a row of the spectrogram matrix), the amplitude vectors are resampled one-by-one in time. The missing samples are obtained by finding the linear function between two time-consecutive data samples, similarly a linear interpolation. Note that due to the linear interpolation of the resampling, the time is normalised for each sub-spectrogram, where 0 is the beginning of each cardiac cycle and 1 is the end of each cardiac cycle. This resampling ensures the same number of samples for each cardiac cycle and thus converts pseudo-cyclostationary spectrogram into a cyclostationary spectrogram. Therefore, for a frequency f of a sub-spectrogram, only time is elongated by resampling (for example in Figs. 3c, e, g). Note that, now, the sample number in time is at least equal to that of the longest cardiac cycle. However, if this resampling changes the size of the cardiac cycle more than 100%, the cardiac cycle is removed. Moreover, if the cardiac cycles are undetectable, as in an arrhyth-

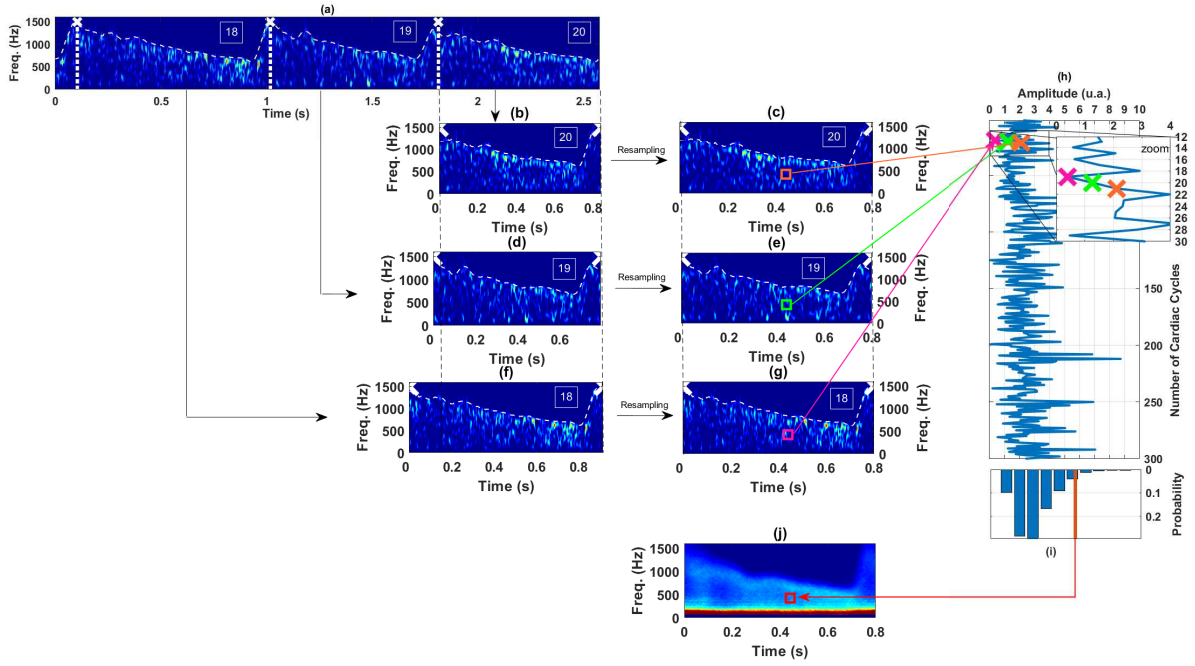

Figure 3: Example of segmentation and duration normalisation of the spectrogram following the cardiac cycles. (a) Non-segmented clean spectrogram $ID_{Emb}(n, f)$. As an illustration, from methods described in section 2.2, the time boundaries of cardiac cycles were depicted by white crosses and the number of cardiac cycles is written in the white boxes. (b), (d) and (f) Sub-spectrograms segmented by the three respective cardiac cycles from the time boundaries of cardiac cycles. (c), (e) and (g) Resampling of the three sub-spectrograms $ID_{Emb,segm}(n, f)$ shown respectively in (b), (d) and (f). These new sub-spectrograms are now normalised in time. Note that they have the same duration to guarantee the cyclostationarity. (h) Example of an amplitude extraction from time-normalised sub-spectrograms for a frequency and time position: amplitude signal as a function of cardiac cycles. The example values from sub-spectrograms (c), (e) and (g) are extracted and depicted respectively in pink, green and orange. (i) Histogram of the amplitude signal shown in (h). A threshold in red is deduced as a percentile of this histogram. (j) 2D-adaptive threshold $\lambda_{Emb}(n, f)$ obtained for all the time positions in the cardiac cycle and for all frequencies. For example, the threshold deduced in (h) (for the region studied in the boxes in (c), (e) and (g)) are reported in the red box. Note that the colormap is the same for all graphs as in Fig. 2.

mia phase, the Doppler signal is excluded over five seconds (from our experience). Finally, the clean spectrograms $ID_{Emb}(n, f)$ and the spectrograms $ID_{Art}(n, f)$ of each cardiac cycle are thus segmented and time-normalised: the new sub-spectrograms $ID_{Emb,segm}(n, f)$ and $ID_{Art,segm}(n, f)$ of each cardiac cycle have the same duration and can be superimposed.

2.3. Two-Dimensional-Adaptive Thresholding

As shown in step 3 in the flow chart shown in Fig. 1, the process of microembolus detection consists of (i) detecting the over intensities of the time-normalised and clean sub-spectrogram $ID_{Emb,segm}$ for each valid cardiac cycle (blue functions in Fig. 1) and of (ii) checking if the HITS is not an artefact (yellow functions in Fig. 1), as follows:

$$\left(ID_{Emb,segm} \underset{H_{Emb}=0}{\overset{H_{Emb}=1}{\gtrless}} \lambda_{Emb}\right) \text{ AND NOT } \left(ID_{Art,segm} \underset{H_{Art}=0}{\overset{H_{Art}=1}{\gtrless}} \lambda_{Art}\right) \quad (6)$$

If the clean sub-spectrogram $ID_{Emb,segm}(n, f)$ is higher than the threshold $\lambda_{Emb}(n, f)$, then the microembolus detector triggers (hypothesis where $H_{Emb} = 1$), otherwise no microembolus detection takes place (hypothesis where $H_{Emb} = 0$). The same principle is applied to artefact rejection: if the sub-spectrogram $ID_{Art,segm}(n, f)$ is higher than the threshold $\lambda_{Art}(n, f)$, then the artefact rejection triggers (hypothesis where $H_{Art} = 1$). Thus, if the clean sub-spectrogram $ID_{Emb,segm}(n, f)$ triggers the first detector without the sub-spectrogram $ID_{Art,segm}(n, f)$ triggering the second detector, a microembolic event is detected. Note that the time-normalised sub-spectrograms are used twice in order to: (1) propose thresholds from all the collection

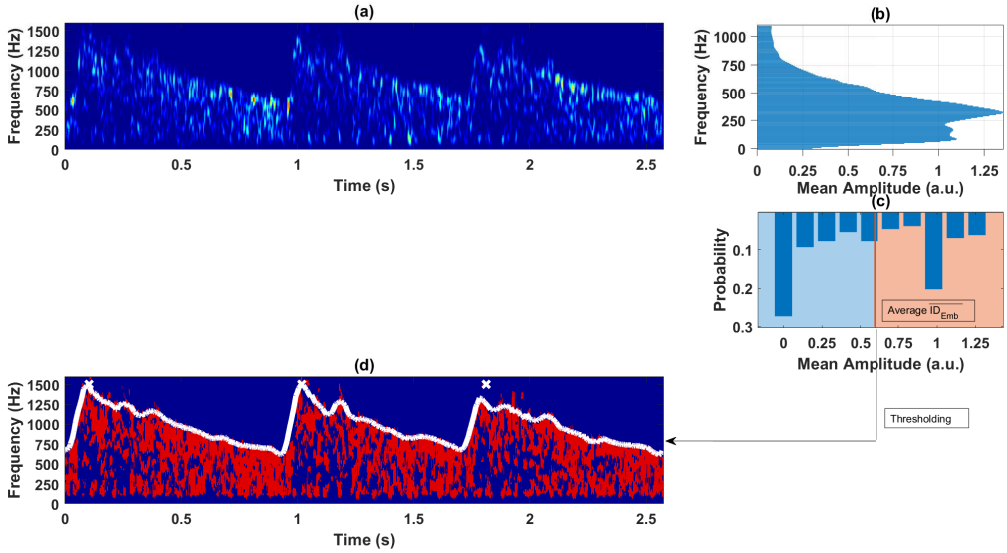

Figure 4: Example of the process to find the time-boundaries of the cardiac cycles. (a) Non-segmented clean spectrogram $ID_{Emb}(n,f)$. (b) Mean Spectrum: average of $ID_{Emb}(n,f)$, $\forall f$. (c) Histogram of the mean spectrum. The threshold $\overline{ID_{Emb}}$ shown with the red line. (d) Binary spectrogram by thresholding $ID_{Emb}(n,f)$ with $\lambda_{Emb}(n,f)$ to detect blood energy (without taking into account the possible presence of microemboli). Note also that the binary spectrogram is red for the area of blood energy if $ID_{Emb}(n,f) \geqslant \overline{ID_{Emb}}$ and blue for the basic area of noise if $ID_{Emb}(n,f) < \overline{ID_{Emb}}$.

of time-normalised sub-spectrograms, (2) detect microemboli from time-normalised sub-spectrograms individually. An example of this step is illustrated in Fig. 5.

First, as defined in eq. 6, the time-normalised and clean sub-spectrograms $ID_{Emb,segm}(n,f)$ are individually compared to the 2D-adaptive threshold $\lambda_{Emb}(n,f)$, for each time n and each frequency f. This 2D-adaptive threshold $\lambda_{Emb}(n,f)$ is deduced from statistical laws of the time-normalised sub-spectrograms for each time n and frequency f (as for example in Fig. 3). For k valid[3] cardiac cycles (as for example, from 1 to 300 in Fig. 3h), for each time position n_k in the cardiac cycle and each frequency f_k (as shown in Figs 3c, e, g), the amplitude A_k is extracted. Note that this signal (with 300 samples in Fig. 3h) looks like a random variable from which the 2D-adaptive thresholds $\lambda_{Emb}(n,f)$ and $\lambda_{Art}(n,f)$ are computed, and where the HITS are statistically rare events. Moreover, to avoid assumptions on the statistics of the time-normalised sub-spectrograms, the 2D-adaptive threshold $\lambda_{Emb}(n,f)$ corresponds to a percentile of the amplitudes of the time-normalised sub-spectrograms, as shown in Fig. 3:

$$\lambda_{Emb}(n,f) = \mathcal{P}\left(ID_{Emb,segm}(n,f), \mathrm{erf}\left(\frac{\mu_{Emb}}{\sqrt{2}}\right)\right), \forall n, \forall f, \tag{7}$$

where μ_{Emb} is the setting parameter of the 2D-adaptive threshold for microembolus detection. Note that the parameter μ_{Emb} is set during a training phase described in subsection 2.5.

Secondly, before identifying each event as microembolus, the method has to check, if the HITS is not an artefact, as defined in eq. 6. From the time-normalised sub-spectrogram $ID_{Art,segm}(n,f)$, the 2D-adaptive threshold $\lambda_{Art}(n,f)$ is computed such as:

$$\lambda_{Art}(n,f) = \mathcal{P}\left(ID_{Art,segm}(n,f), \mathrm{erf}\left(\frac{\mu_{Art}}{\sqrt{2}}\right)\right), \forall n, \forall f, \tag{8}$$

where μ_{Art} is the setting parameter of the 2D-adaptive threshold for artefact rejection. Note that the parameter μ_{Art} is set during a training phase described in subsection 2.5.

Moreover, a HITS often appears with multiple spots in the same area in the sub-spectrogram, similar to the two spots in the example shown in Fig. 5c. However, only one detection should be counted. Thus, multiple close detections must be combined to avoid multiple countings. In image processing,

[3]It is obvious that the computation of the 2D-adaptive threshold $\lambda_{Emb}(n,f)$ is made from all sub-spectrograms except those ones removed during the segmentation step.

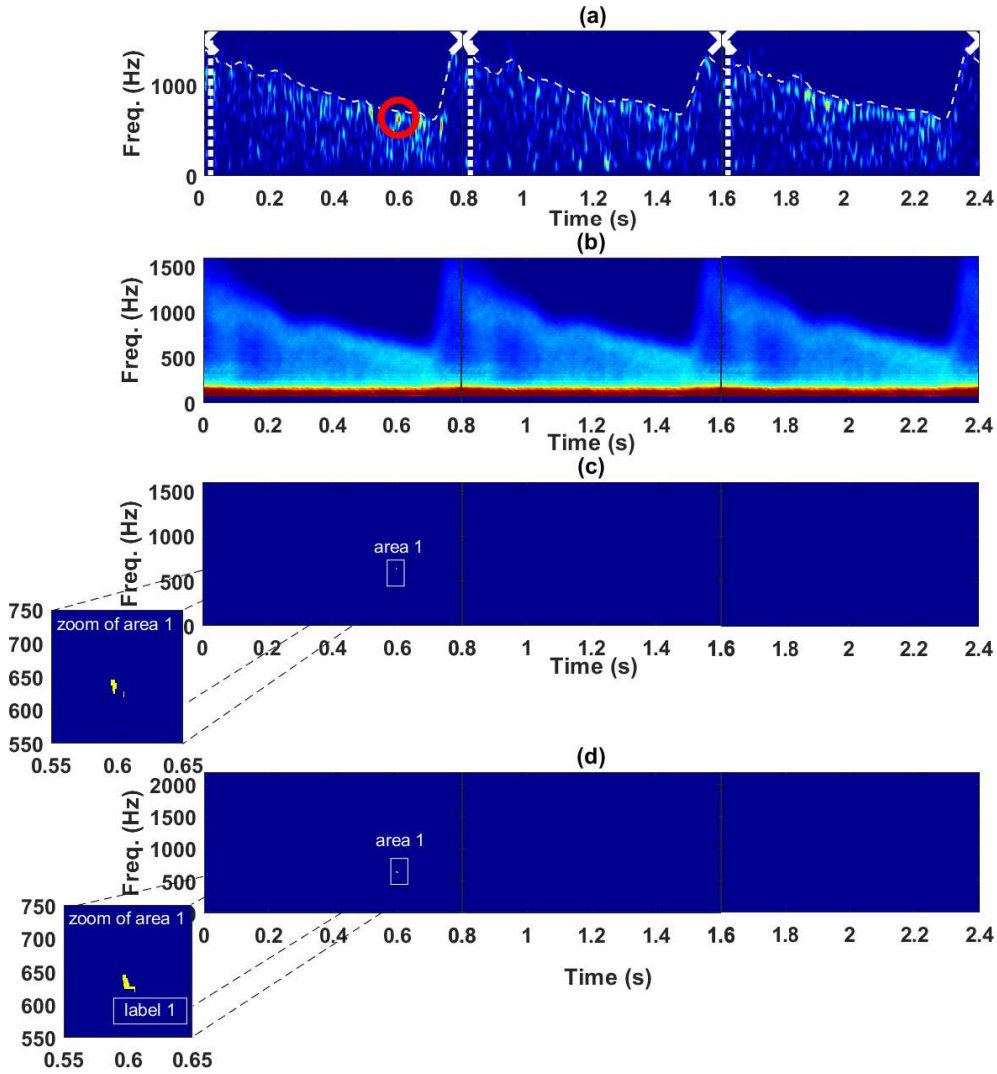

Figure 5: Example of microembolus detection. (a) Time-normalised and clean sub-spectrograms $ID_{Emb,segm}(n,f)$. A microembolus example is encircled in red, and the time boundaries of cardiac cycles are depicted by white crosses. (b) Threshold $\lambda_{Emb}(n,f)$. Note that the threshold $\lambda_{Emb}(n,f)$ is repeated for the entire cardiac cycle. (c) Thresholding of $ID_{Emb,segm}(n,f)$ by $\lambda_{Emb}(n,f)$. A zoom is done around the detection. (d) Detection from (c) after the closing morphological operation and labelling. A zoom is applied around the same detection. The label of the detected area is written in a white box.

this merging is done using a closing morphological[4] operation [33] on $H_{Emb}(n,f)$ and on $H_{Art}(n,f)$ by using a structuring element B. Note that the size of B has been evaluated throughout the gold standard phase. It corresponds to 6% of the longest cardiac cycle duration along the x-axis and 12% of sampling frequency along the y-axis.

Finally, the events detected from $ID_{Emb,segm}(n,f)$ are compared with those detected from $ID_{Art,segm}(n,f)$ to reject artefacts (eq. 6). The events of $ID_{Emb,segm}(n,f)$ which have no common point in time and frequency are kept. The events are counted from a labelling algorithm of connected components[5] to 8 connections [34].

[4]The closing operation of the binary image I with the structuring element B consists in a dilatation operation following an erosion operation, such $I \bullet B = (I \oplus E_s) \ominus E_s$ with the dilatation $I \oplus B = \{i + b \mid b \in B, i \in I\}$ and the erosion $I \ominus B = \{i \mid B_i \subset I\}$.

[5]The principle of algorithm consists in (1) browsing all unlabelled positive pixels (positive detection with a value of 1), (2) associating the positive neighbouring pixels following the 8 possible directions from the pixel, (3) repeat the previous operations until all positive pixel has a label. Finally, by counting the label amount, the algorithm can give the number of regions.

2.4. Acquisition of Doppler Signals

The Doppler signals analysed in this study were recorded, in a non-interventional practise, by a Holter TCD (TCD-X, Atys Medical, Soucieu-en-Jarrest, France), without online detection. An ultrasound wave with a 1.5 MHz frequency was transmitted to the middle cerebral artery of patients with carotid artery stenosis. To guarantee the absence of energy measured in the negative frequencies of the spectrogram (*i.e.* backward flow), the clinician has to find a good location with a good angle. Note that the good positioning is in the middle cerebral artery [35], where backward flow was never present. The pulse repetition frequency (PRF) was 6.4 kHz and the ultrasound power was 150 mW/cm^2.

These clinical recordings were carried out at the Hospital of Lille (Centre Hospitalier Regional Universitaire de Lille, Lille, France) approved by its research ethics council. All medical acts are performed in the usual way, without any additional or unusual procedure for diagnosis, treatment or monitoring. Therefore, here, the recording analysis is a retrospective study where the results have no interference with patient care.

Only recordings from patients with asymptomatic high-grade carotid stenosis were kept. We also excluded from the database the recordings from patients with absence of an acoustic window necessary for TCD and without non-biological prosthetic heart valves.

After the clinical exam, these audio files were played and their respective spectrograms were visualized to constitute the gold standard of the detection. Microembolus signatures were manually identified based on their audible characteristics and a visual inspection of the spectrogram [36] by three blinded observers of our laboratory. These microembolus signatures could be detected equally by both experts and non-experts, since the experience level of the experts is not considered as a critical factor [27, 37]. Thus the time positions of microembolus events found by all observers were recorded. Note that listening was performed twice: first at the normal speed and second at the half normal speed. Indeed, listening at half the normal speed allows us to overcome the well-known temporal and frequency masking effects in audio files, which assures detecting several microemboli previously inaudible at normal speeds. Furthermore, each microembolus detected could be gaseous or solid, without differentiation of the microembolus nature.

2.5. Database and Validation

The post-processing phase was performed with a standard personal computer from which the Holter recordings were converted into audio-wave files with a sampling frequency of 4.4 kHz. The whole method of microembolus detection is developed with Matlab (The Mathworks, Natick, MA, USA). It was tested on 38 signals recorded from 38 patients for about 64 $\pm$ 7 minutes (*i.e.* 1 Doppler signal per patient) with a signal-to-noise ratio between 12 and 32 dB. Note that the size of this dataset is similar to previous studies [14, 22, 23]. This database is divided into two groups: 15 signals for the training phase and 23 signals for the testing phase. Also note that these signals were randomly distributed in both groups.

Taking into consideration the high amount of artefacts and the long duration of recordings, every signal was cut into five-minute dataset, to remove the loss of blood flow signal. Note that, because of the resampling step, if the cardiac rhythm changes highly or if the patient has strong arrhythmia, the time-normalisation may deform slightly the spectrogram and the HITS. To limit this distortion, the duration between two resets may be shorter than the five minutes used in this study. The spectrograms of these five-minute signals described from eq. 1 were then computed with $N = 64$ with an overlap of 80% and a zero padding of 512, according to the previous recommendations [25]. Each part of the five-minute signal was analysed separately and independently. Note that this slicing allowed us to limit the impacts of modifications of signal dynamic range and the cardiac rhythm, and the potential loss of blood flow signal. Finally, the five-minute signals were analysed for microembolus detection.

During the training phase, the 2D-adaptive thresholds $\lambda_{Emb}(n,f)$ and $\lambda_{Art}(n,f)$ are empirically decreased using the parameters μ_{Emb} and μ_{Art} in order to obtain the best compromise between the false alarm rate FAR and the detection rate DR. For each signal, we counted the number of true positive TP and the number of false positive FP for the standard method and for the 2D-adaptive method proposed here. The detection rate[6] $DR_{(\%)}$ and the false alarm rate[7] $FAR_{(\%)}$ were thus deduced as:

$$DR_{(\%)} = 100 \cdot \frac{TP}{D_{emb}} \quad \text{and} \quad FAR_{(\%)} = 100 \cdot \frac{FP}{D_{tot}}, \tag{9}$$

[6] Rate of good detection, *i.e.* a detection is a real microembolus, among all real microemboli

[7] Rate of wrong detection, *i.e.* a detection is not a real microembolus, among all detections

where D_{emb} is the number of real microemboli counted in the gold standard, D_{tot} the total number of detections. In the last step, during the testing phase, the 2D-adaptive thresholds $\lambda_{Emb}(n,f)$ and $\lambda_{Art}(n,f)$ were not changed in assessing the 2D-adaptive method.

For comparison, another analysis was done with the same protocol, but with the most commonly used standard method to detect the presence of microemboli. The detection is usually based on the energy associated with a constant threshold [27]. Note that the detection in commercial device is based on the maximum short-term power spectrum $ID_{Emb,stand}$:

$$ID_{Emb,stand}(n) = \sum_{f} S(\mathbf{y}, n, f). \tag{10}$$

The standard constant threshold $\lambda_{Emb,stand}(n)$ is thus set above the maximal detected energy of the Doppler signal when no embolus is present:

$$\lambda_{Emb,stand} = 10{\cdot}\log_{10}\left(\max\left[ID_{Emb,stand}(n)\right]\right) + \mu_{Emb,stand} \tag{11}$$

Note that for this standard detection, the artefact was manually rejected.

Finally, to evaluate the detection performance of the detection of the weakest microemboli, the "embolus-to-blood ratio" (EBR) is assessed. EBR indicates how strong an embolic signal is relative to the background Doppler signal, such as:

$$EBR = 10\log_{10}\left(\frac{P_{E+B}}{P_B}\right), \tag{12}$$

where P_{E+B} is the backscattered power measured when an embolus and the blood are present in the Doppler sample volume, P_B the backscattered power measured from blood alone in the sample volume [18]. Note that we can presume that the higher the EBR, the bigger the microembolus [38].

3. Results

In this part, we present the results of the microembolus detections during the training and testing phases. First, we determine the best training phase settings. Second, we compare the results obtained in the testing phase from the new 2D-adaptive detector and from the results of the standard detector, to evaluate the performance of this new 2D-adaptive detector.

The training phase allowed us to set the thresholds by finding the best compromise between both the false alarm rate FAR and detection rate DR. Fig. 6 shows the detection rates as a function of the false alarm rates obtained from several selected threshold values for the standard detector (Fig. 6b) and the 2D-adaptive detector (Fig. 6a). The ROC curve of the new detector is closest to the ideal point (0% FAR and 100% DR). The highest performance of new detector was obtained with the thresholds for microembolus detection $\mu_{Emb} = 2.5$ (eq. 7) and for artefact rejection $\mu_{Art} = 5$ (eq. 8). It is three times higher ($d_{adapt}/d_{stand} = 56.1/18.9$) than the best performance obtained for the standard detector with $\mu_{Emb,stand} = 5$. This result is confirmed by the area under the ROC curve (AUC), which is 3.6 times closer to the ideal AUC (comparison of the white areas in Fig. 6: $(100-58.8)/(100-88.6)$) in comparison with that of the standard detector. Note that the AUC has to tend to 100% for optimal detection.

In Fig. 7, we reported the detection rate and the false alarm rate during the training and the testing phases obtained with the best thresholds shown in Fig. 6. As an illustration, we showed these rates for the standard method for its training and testing phases. Moreover, the rate of invalid cardiac cycles correctly rejected (for artefact and strong arrhythmia) was compared to the rate of non-rejected invalid cardiac cycles.

The detection rate increased and the false alarm rate decreased with the 2D-adaptive method in comparison to the standard method. First, between the training and the testing phases, the performances were very close, because our dataset had to be homogeneous. Second, the detection rate was increased by 22% (83% − 61%) in comparison to the standard method. Moreover, the false alarm rate was reduced by 28% (45% − 17%). However, for the standard detector, note that artefacts were manually excluded. The comparison remains relative, due to the addition of the artefact rejection method. Here, the false alarm rate of the standard method can be considered less penalised than that of our proposed method, since the performance of manual rejection is better than that of the proposed rejection method.

Finally, Fig. 7 shows that the time boundaries of 24% (23+1) cardiac cycles were impossible to assess. Therefore, they should be rejected. However, only 23% of cardiac cycles were correctly rejected. The time boundaries of only 1% cardiac cycles were not correctly assessed and hence not rejected. These errors increased the false alarm rate by 3% only. Note also that, among these 24% of cardiac cycles highly corrupted by artefacts, microemboli are rare

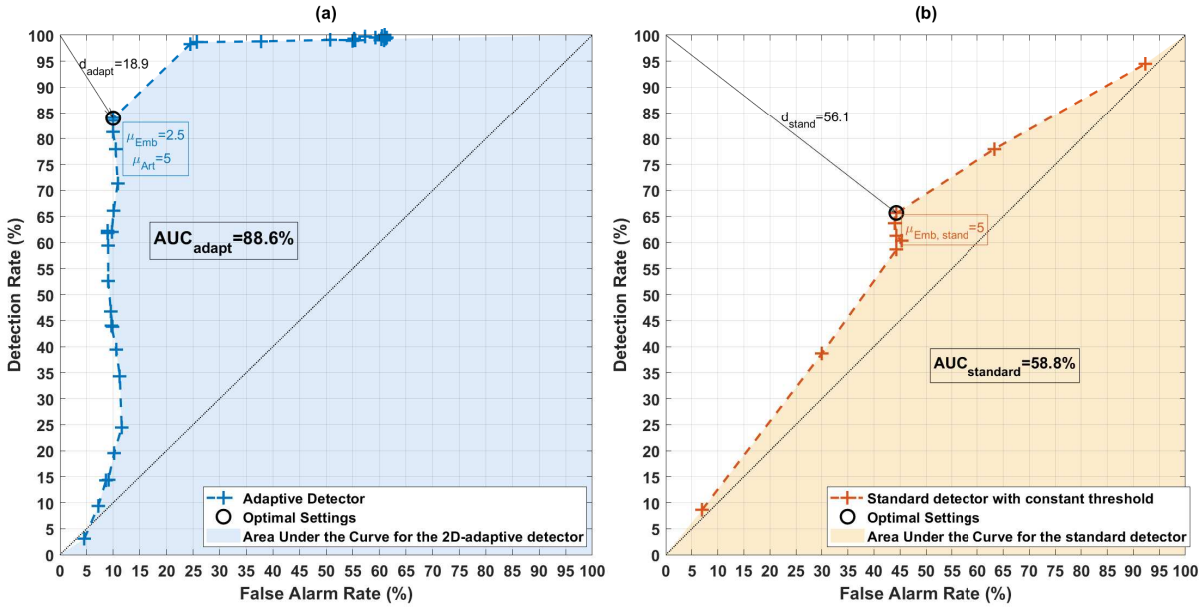

Figure 6: ROC curves of the 2D-adaptive detector (a) and the standard detector (b) during the testing phase: detection rates as a function of false alarm rates obtained from several thresholds of microembolus detection μ_{Emb} (eq. 7) and of artefact rejection μ_{Art} (eq. 8). Note that the ideal point is for 0% FAR and 100% DR.

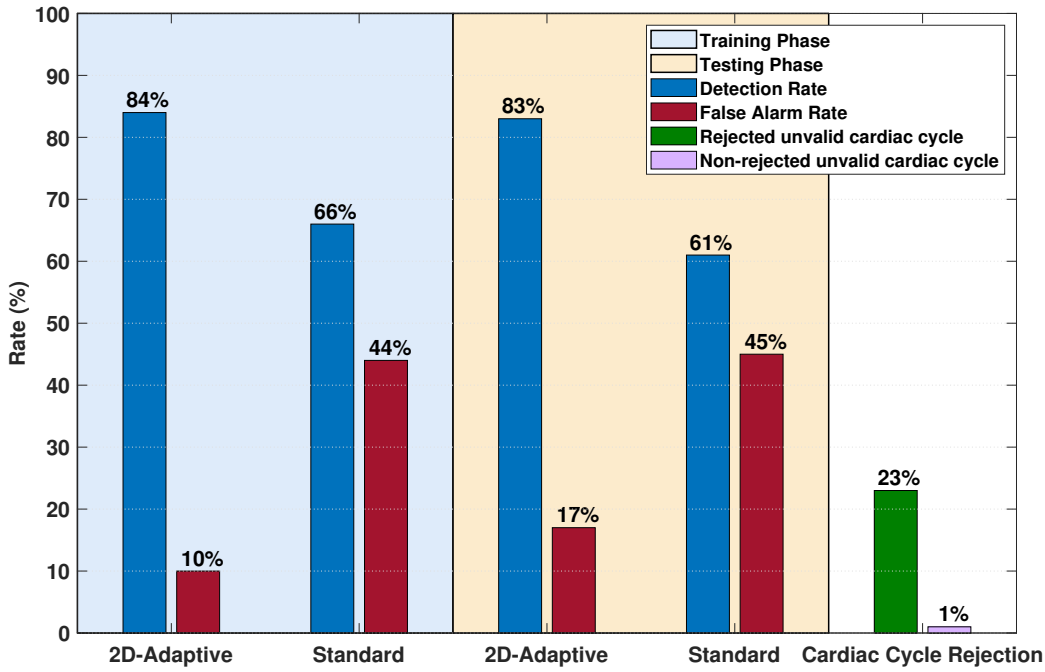

Figure 7: Detection rate and false alarm rate of the 2D-adaptive method for both training and testing phase. As an illustration, these values are compared with the rates obtained to the standard detector. The rate of invalid cardiac cycle correctly rejected is shown in green and the rate of invalid cardiac cycle non-rejected in purple.

and undetectable, even manually, because drown in artefacts.

As an illustration, in Fig. 8, the histogram of the rate of microemboli detected (*i.e.* the ratio between the number of microemboli for an EBR and the total number of microemboli detected by the gold standard) is reported as a function of the embolus-to-blood ratio (EBR), by the 2D-adaptive method (Fig. 8a), by the standard method (Fig. 8b), and by the gold standard (Fig. 8c) along with those that are undetected (Fig. 8d):

- 61% of microemboli in our database had an EBR higher than 24 dB. These microemboli were detected by both the 2D-adaptive method and standard method;
- 38% of microemboli in our database had an EBR between 15 and 24 dB. They could be detected only with the 2D-adaptive method, even though 40% of microemboli with an EBR below 19 were still undetectable;
- 1% of microemboli in our database had an EBR lower than 15 dB and were undetectable.

The new method was more efficient, because it detect more microemboli (88% *vs.* 61%), especially those having smaller EBR. It may be more efficient for microemboli with smaller sizes.

4. Discussions and Conclusion

The 2D-adaptive detector based on the time-normalised sub-spectrogram analysis has been proposed as a method to overcome limitations of standard energy detectors. This new detector allows improving the performance of microembolus detection while reducing the false alarm rate. Moreover, the new detector could detect microemboli weaker than those detected by the standard method. These performances were made possible by proposing the 2D-adaptive threshold in both time and frequency, adjusted every five minutes and for every patient. As long as the segmentation of the spectrogram is possible, this 2D-adaptive time-frequency threshold will be at the origin of detecting weaker microemboli. The segmentation of the spectrogram was guaranteed by the pseudo-cyclostationarity property and by the relatively rare microembolic events. The cardiac cycle time boundaries were assessed. Although a false alarm could occur due to artefacts at the time boundaries of the cardiac cycle, its rate was highly reduced. This showed that our detector was effective. Therefore, the analysis of long acquisitions could be possible, because the new detector integrates an artefact rejection. Nevertheless, since the new detector was designed to take into account the features of mono-gated Holter TCD, the artefact rejection proposed here is valid only if the blood flow is forward as in the case of our database with carotid stenosis. As soon as this assumption is invalid, *e.g.* by aliasing which can be generating by intracranial stenosis, the artefact rejection method should be changed (manual or automatic) and the microembolus detection in the forward flow should be extended to backward flow.

No hypothesis about statistical distribution of data was required, due to threshold settings being based on percentile. However, the settings of the detection had to be optimised during a training phase. Note that, as for all detection methods based on a threshold set by a parameter, the gain of performances did not depend only on the method (*e.g* segmentation step), but also on data from which the threshold is computed. For instance, inter and intra variations between patients or variations in signatures of microemboli must affect the threshold; *i.e.* in this study, the Doppler signals used in the training phase was done randomly.

Finally, the method has been designed for offline detection meaning that the computational cost is not an issue, and so it seems to be particularly adapted on long Doppler signal acquired with a mono-gated Holter TCD.

The long duration of acquisition would increase the number of occurrences and thus increase the diversity of microembolic signatures (weak and high EBR). The analysis of these long duration acquisitions may provide more realistic information closer to the living conditions of patients to improve the diagnostic.

Acknowledgements

The authors would like to acknowledge Marilys Almar and Benoît Guibert (Atys Medical, Soucieu-en-Jarrest, France) for the Holter TCD. They also thank Corinne Gautier (Centre Hospitalier Regional Universitaire de Lille, Lille, France) for the Doppler Data.

This work was supported by Agence Nationale de la Recherche (Project ANR-2010-TECS-006-02, EMBOLTER, Mean time ambulatory emboly counting for stroke risk evaluation).

[1] R. Shah, E. Wilkins, M. Nichols, P. Kelly, F. El-Sadi, F. L. Wright, N. Townsend, Epidemiology report: trends in sex-specific cerebrovascular disease mortality

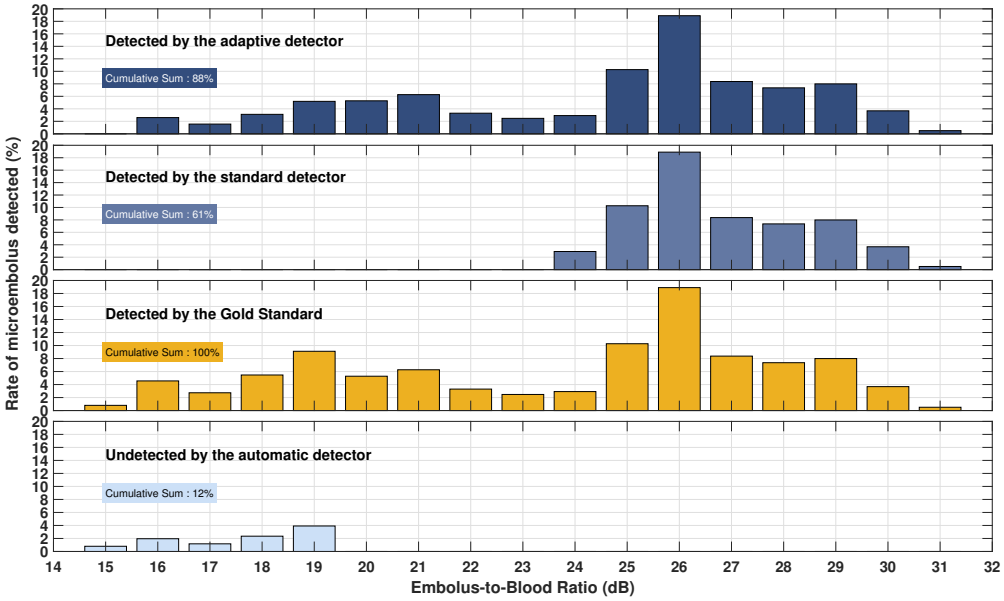

Figure 8: Histogram of the microembolus detected (a) by the 2D-adaptive method, (b) by the standard method, (c) by the gold standard and (d) undetected, as a function of the embolus-to-blood ratio (EBR).

in Europe based on who mortality data, European heart journal 40 (9) (2018) 755–764.

[2] E. Wilkins, L. Wilson, K. Wickramasinghe, P. Bhatnagar, J. Leal, R. Luengo-Fernandez, R. Burns, M. Rayner, N. Townsend, European cardiovascular disease statistics 2017, European Heart Network, Brussels, Belgium, 2017.

[3] D. W. Droste, E. B. Ringelstein, Detection of high intensity transient signals (hits): How and why?, European journal of ultrasound 7 (1) (1998) 23–29.

[4] M. P. Spencer, G. I. Thomas, S. C. Nicholls, L. R. Sauvage, Detection of middle cerebral artery emboli during carotid endarterectomy using transcranial Doppler ultrasonography., Stroke 21 (3) (1990) 415–423.

[5] V. Vuković-Cvetković, Microembolus detection by transcranial doppler sonography: review of the literature, Stroke research and treatment 2012 (2011) 7.

[6] M. Siebler, A. Nachtmann, M. Sitzer, G. Rose, A. Kleinschmidt, J. Rademacher, H. Steinmetz, Cerebral microembolism and the risk of ischemia in asymptomatic high-grade internal carotid artery stenosis, Stroke 26 (11) (1995) 2184–2186.

[7] H. S. Markus, A. King, M. Shipley, R. Topakian, M. Cullinane, S. Reihill, N. M. Bornstein, A. Schaafsma, Asymptomatic embolisation for prediction of stroke in the asymptomatic carotid emboli study (aces): a prospective observational study, The Lancet Neurology 9 (7) (2010) 663–671.

[8] V. G. Dunne, M. l. Besser, W. J. Ma, Transcranial doppler in carotid endarterectomy, Journal of clinical neuroscience 8 (2) (2001) 140–145.

[9] A. D. Mackinnon, R. Aaslid, H. S. Markus, Long-term ambulatory monitoring for cerebral emboli using transcranial doppler ultrasound, Stroke 35 (1) (2004) 73–78.

[10] R. Brucher, D. Russell, Automatic online embolus detection and artifact rejection with the first multifrequency transcranial doppler, Stroke 33 (8) (2002) 1969–1974.

[11] S. Marvasti, D. Gillies, F. Marvasti, H. S. Markus, Online automated detection of cerebral embolic signals using a wavelet-based system, Ultrasound in medicine & biology 30 (5) (2004) 647–653.

[12] M. Gençer, G. Bilgin, N. Aydin, Embolic doppler ultrasound signal detection via fractional Fourier transform, in: Annual International Conference of the IEEE Engineering in Medicine and Biology Society, 2013, pp. 3050–3053.

[13] L. Fan, E. Boni, P. Tortoli, D. H. Evans, Multigate transcranial doppler ultrasound system with real-time embolic signal identification and archival, IEEE transactions on ultrasonics, ferroelectrics, and frequency control 53 (10) (2006) 1853–1861.

[14] N. Aydin, F. Marvasti, H. S. Markus, Embolic doppler ultrasound signal detection using discrete wavelet transform, IEEE Transactions on Information Technology in Biomedicine 8 (2) (2004) 182–190.

[15] P. Sombune, P. Phienphanich, S. Phuechpanpaisal, S. Muengtaweepongsa, A. Ruamthanthong, P. De Chazal, C. Tantibundhit, Automated cerebral emboli detection using adaptive threshold and adaptive neuro-fuzzy inference system, IEEE Access 6 (2018) 55361–55371.

[16] M. Geryes, S. Ménigot, J. Charara, M. Nasserdine, A. Mcheick, J.-M. Girault, Enhanced weak doppler micro-embolic signal detection using energy fluctuations, Biomedical Signal Processing and Control 47 (2019) 177–182.

[17] X. Lei, Z. Heng, G. Shangkai, Barker code in tcd ultrasound systems to improve the sensitivity of emboli detection, Ultrasound in medicine & biology 35 (1) (2009) 94–101.

[18] J.-M. Girault, D. Kouamé, A. Ouahabi, F. Patat, Microemboli detection: an ultrasound Doppler signal processing viewpoint, IEEE Transactions on biomedical Engineering 47 (11) (2000) 1431–1439.

[19] M. Geryes, S. Ménigot, W. Hassan, A. Mcheick,

J. Charara, J.-M. Girault, Detection of doppler microembolic signals using high order statistics, Computational and Mathematical Methods in Medicine 2016 (2016) 8.

[20] J.-M. Girault, M. Biard, D. Kouamé, A. Bleuzen, F. Tranquart, Spectral correlation of the embolic blood doppler signal, in: IEEE International Conference on Acoustics Speech and Signal Processing Proceedings, Vol. 2, 2006.

[21] S. Ménigot, L. Dreibine, N. Meziati, J.-M. Girault, Automatic detection of microemboli by means of a synchronous linear prediction technique, in: IEEE International Ultrasonics Symposium, IEEE, 2009, pp. 2371–2374.

[22] B. K. Guepie, M. Martin, V. Lacrosaz, M. Almar, B. Guibert, P. Delachartre, Sequential emboli detection from ultrasound outpatient data, IEEE Journal of Biomedical and Health Informatics PP (99) (2018) 1–1.

[23] B. K. Guépié, B. Sciolla, F. Millioz, M. Almar, P. Delachartre, Discrimination between emboli and artifacts for outpatient transcranial doppler ultrasound data, Medical & Biological Engineering & Computing 55 (10) (2017) 1–11.

[24] D. G. Grosset, D. Georgiadis, A. W. Kelman, K. R. Lees, Quantification of ultrasound emboli signals in patients with cardiac and carotid disease., Stroke 24 (12) (1993) 1922–1924.

[25] N. Aydin, H. S. Markus, Optimization of processing parameters for the analysis and detection of embolic signals, European Journal of ultrasound 12 (1) (2000) 69–79.

[26] H. Markus, A. Loh, M. M. Brown, Computerized detection of cerebral emboli and discrimination from artifact using doppler ultrasound., Stroke 24 (11) (1993) 1667–1672.

[27] E. B. Ringelstein, D. W. Droste, V. L. Babikian, D. H. Evans, D. G. Grosset, M. Kaps, H. S. Markus, D. Russell, M. Siebler, et al., Consensus on microembolus detection by tcd, Stroke 29 (3) (1998) 725–729.

[28] L. Y. L. Mo, L. C. M. Yun, R. Cobbold, Comparison of four digital maximum frequency estimators for Doppler ultrasound, Ultrasound in Medicine & Biology 14 (5) (1988) 355–363.

[29] A. H. Steinman, J. Tavakkoli, J. G. Myers, R. S. C. Cobbold, K. W. Johnston, A new approach for determining maximum frequency in clinical doppler ultrasound spectral estimates, in: Proceedings of the 22nd Annual International Conference of the IEEE Engineering in Medicine and Biology Society, Vol. 4, Chicago, IL, USA, 2000, pp. 2640–2643.

[30] E. Billauer, Peakdet: peak detection using matlab (Jul. 2012).
URL `http://www.billauer.co.il/peakdet.html`

[31] H. Tanaka, K. D. Monahan, D. R. Seals, Age-predicted maximal heart rate revisited, Journal of the American College of Cardiology 37 (1) (2001) 153–156.

[32] G. Dolecek, Random signals and processes primer with MATLAB, Springer, New York, NY, 2013.

[33] J. Serra, Image analysis and mathematical morphology, Academic Press, London, UK, 1982.

[34] R. C. Gonzalez, R. E. Woods, S. L. Eddins, Digital Image Processing Using MATLAB, 2nd Edition, Gatesmark Publishing, 2009.

[35] E. M. L. Chung, J. P. Hague, M.-A. Chanrion, K. V. Ramnarine, E. Katsogridakis, D. H. Evans, Embolus trajectory through a physical replica of the major cerebral arteries, Stroke 41 (4) (2010) 647–652.

[36] M. A. Moehring, A. S. Dewaraja, T. O. Mera, M. P. Spencer, System and method for grading microemboli monitored by a multi-gate doppler ultrasound system, US Patent 7,771,358 (Aug. 2010).

[37] E. Chung, L. Fan, C. Degg, D. H. Evans, Detection of doppler embolic signals: psychoacoustic considerations, Ultrasound in medicine & biology 31 (9) (2005) 1177–1184.

[38] M. A. Moehring, J. R. Klepper, Pulse doppler ultrasound detection, characterization and size estimation of emboli in flowing blood, IEEE Transactions on Biomedical Engineering 41 (1) (1994) 35–44.

Appendix A. Algorithm

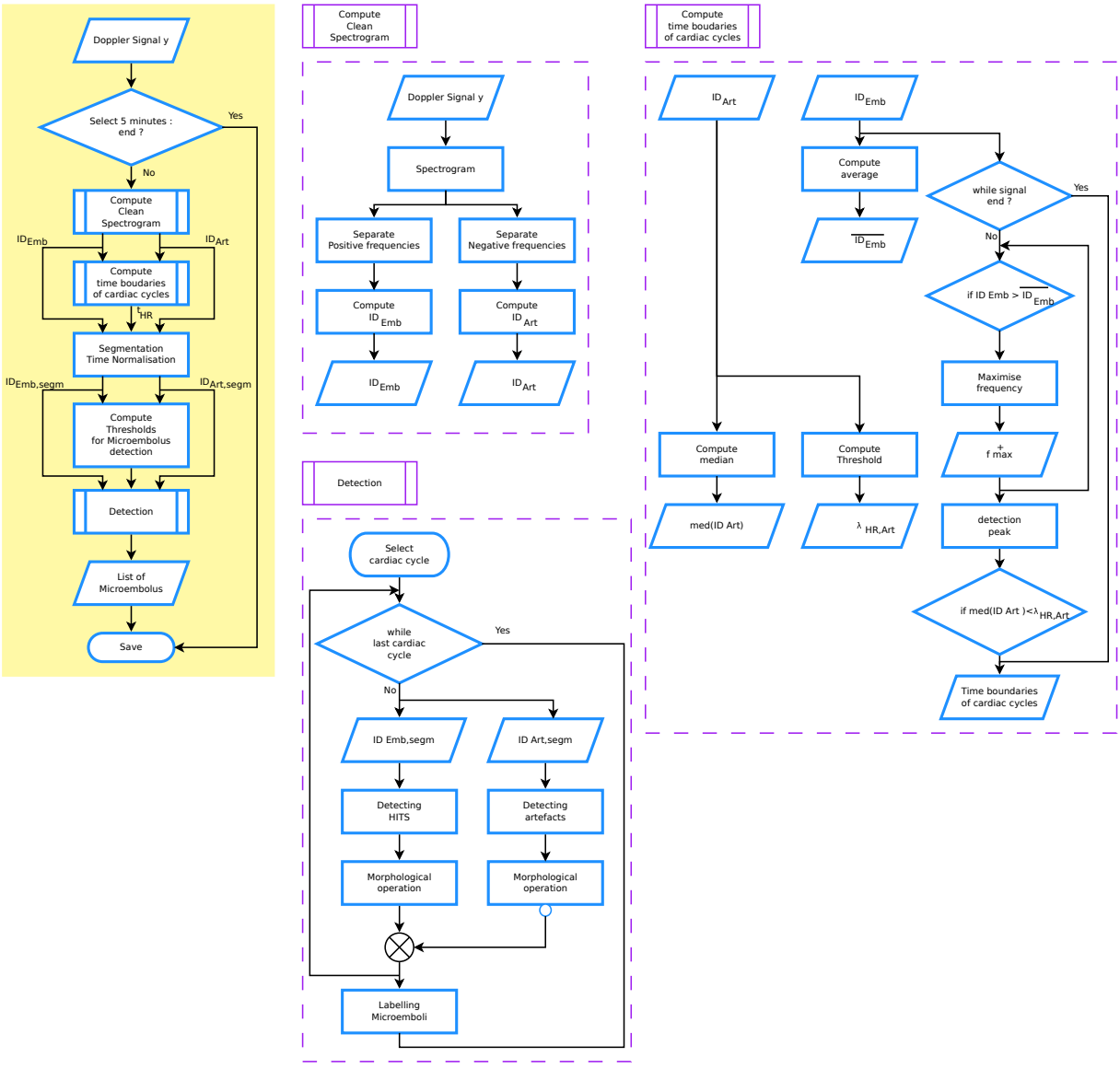

Figure A.9: Detailed flow chart diagram of microembolus detection.